Remote sensing backscattering model for sea ice: Theoretical modelling and analysis

Syabeela Syahali[1] & Hong Tat Ewe[2*]

[1] Faculty of Engineering and Technology, Multimedia University, Jalan Ayer Keroh Lama, Bukit Beruang, Melaka 75450, Malaysia;

[2] Faculty of Engineering and Science, Universiti Tunku Abdul Rahman, Jalan Genting Kelang, Kuala Lumpur 53300, Malaysia

Abstract　Remote sensing has been used in Antarctic studies as an earth observation technique to study the polar region. A remote sensing forward model is an important tool in polar research to study and understand scattering mechanisms and sensitivity of physical parameters of snow and sea ice. In this paper, a reliable theoretical model to study sea ice is developed. The theoretical model in a prior work was improved by including multiple-surface scattering, based on an existing integral equation model and additional second-order surface-volume scattering. This model is applied to a desalinated ice layer above thick saline ice and analyzed using different frequencies, bottom surface roughness and sea-ice layer thickness. Improvement in calculation of the backscattering coefficient of the sea-ice layer is investigated for both co-polarized and cross-polarized returns. The effect on each scattering mechanism is also investigated, to understand in more detail the effect of surface multiple scattering and second-order surface-volume scattering. Comparisons are also made with field measurement results, to validate the theoretical model. Results show improvement in the total backscattering coefficient for cross-polarized return in the studied range, suggesting that multiple-surface scattering and surface-volume scattering up to second order are important scattering mechanisms in the sea-ice layer and should not be ignored in polar research.

Keywords　multiple-surface scattering, surface-volume scattering, backscattering

1　Introduction

Antarctica is important in global climate change. In this fifth largest continent in the world, there is about 19 million square kilometres of sea ice in winter. With its critical role in balancing the global energy distribution, constant monitoring of Antarctic sea ice is crucial to study the effects of global warming. Because of the continent's harsh weather, remote sensing technology is a suitable tool in this endeavour.

In recent years, both active and passive remote sensing satellites have been used for data collection and monitoring of sea ice. For improved interpretation of satellite images, it is important to understand the interaction and scattering mechanisms between electromagnetic waves and snow and sea ice. To achieve this, a reliable forward model should be developed. A remote sensing forward model is also important in polar research to study the sensitivity of physical parameters in this topic, for use in the development of an inverse model of parameter retrieval using microwave remote sensing[1].

In a prior work[2], a backscattering model for an electrically dense medium was developed based on radiative transfer theory[3]. This model assumes that wave-interface effects are due only to single scattering on a surface, and that surface-volume interaction is due only to first-order surface-volume scattering. However, multiple scattering can also contribute to the effect, especially for rough surfaces. Second-order surface-volume scattering may also be important and should not be ignored. Therefore, it is important to develop a model that includes in its surface scattering

formulation the surface multiple-scattering effect together with the surface single-scattering effect, and considers up to second-order surface-volume scattering in its surface-volume formulation.

This paper is an extension of earlier work[4-6], in which a reliable theoretical model of snow and sea ice was developed. The theoretical model was improved[2] by including multiple-surface scattering, based on an existing integral equation model (IEM)[7] and additional second-order surface-volume scattering. We present herein the effect of including these terms on the total backscattering coefficient and on each scattering mechanism, for various frequencies, bottom surface roughnesses and sea-ice layer thicknesses for sea ice. Finally, the developed model is validated to demonstrate its reliability, through comparison with field measurement results.

2 Model configuration

Figure 1 shows a cross section of the layer used in theoretical modelling. The layer is modelled as a discrete inhomogeneous medium of depth d (in m), in which randomly distributed spherical scatterers are embedded. This layer is bounded on top and bottom by irregular surface boundaries. Above the layer is air, and below is a homogenous half space. This medium is considered electrically dense, in which the spacing between scatterers is comparable to wavelength[8].
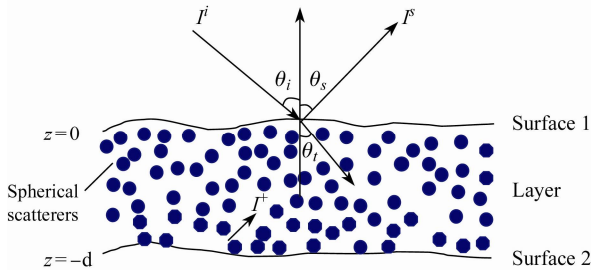

Figure 1   Cross section of the layer.

Surfaces 1 and 2 are rough, with parameters of surface root mean square (rms) height and correlation length. The IEM, which accounts for both single and multiple scattering, is used to model surface scattering[7]. A spherical scatterer is modelled as a Mie scatterer. Parameters such as radius, permittivity and volume fraction are used to configure these scatterers. In an electrically dense medium in which there is more than one scatterer within a wavelength distance, spatial arrangement of the scatterers has been shown to significantly affect their scattering properties[9-12]. These effects are taken into account by applying the Dense Medium Phase and Amplitude Correction Theory (DM-PACT)[9-10] for the phase matrix of the Mie scatterer.

Incident and scattered intensities are labelled as I^i and I^s, respectively. Propagation intensity is split into upward intensity I^+ and downward intensity I^-. This model is suitable for application to the snow and sea ice layer, in which

scatterers are spherical and the layer is electrically dense. We used the parameters for sea ice for the theoretical modelling. The model prediction is then compared with field measurements in sea ice.

3 Model formulation

The radiative transfer equation[3] characterizes propagation and scattering of specific intensities inside a medium, and is given by

$$\cos\theta \, \frac{\mathrm{d}\bar{I}}{\mathrm{d}z} = -\bar{\bar{\kappa}}_e \bar{I} + \int \bar{\bar{P}}\bar{I}\mathrm{d}\Omega \,, \qquad (1)$$

where $\bar{I}$ is the Stokes vector, $\bar{\bar{\kappa}}_e$ is the extinction matrix, and $\bar{\bar{P}}$ is the phase matrix of the medium. The phase matrix $\bar{\bar{P}}$ is

$$\bar{\bar{P}}(\theta,\phi;\theta',\phi') = \langle |\psi|^2\rangle_n \cdot \bar{\bar{S}} = \begin{bmatrix} P_{vv} & P_{vh} \\ P_{hv} & P_{hh} \end{bmatrix}, \qquad (2)$$

where $\langle |\psi|^2\rangle_n$ is the dense-medium phase correction factor[9], and $\bar{\bar{S}}$ is the Stokes matrix with close-spacing amplitude correction[13]. Details of the formulation can be found in Chuah et al.[9].

This radiative transfer equation has been solved up to second order[1]. The solution terms of the equation were then grouped into three major scattering terms contributing to the backscattering return. These are surface scattering, surface-volume scattering and volume scattering.

3.1 Surface scattering

The surface scattering term is the zero-th order solution of Equation (1) and is given by

$$\sigma_{pq}^s = \sigma_{pq}^{s1} + \sigma_{pq}^{s2}, \qquad (3)$$

where σ_{pq}^{s1} and σ_{pq}^{s2} are given by

$$\sigma_{pq}^{s1}(\theta_s,\phi_s;\theta_i,\phi_i) = \sigma_{pq}^{o1}(\theta_s,\phi_s;\theta_i,\phi_i) \qquad (4)$$

and

$$\sigma_{pq}^{s2}(\theta_s,\phi_s;\theta_i,\phi_i) = \cos\theta_s T_{01}(\theta_s,\theta_{1s})T_{10}(\theta_{1t},\theta_i)$$
$$\cdot \sec\theta_{1s} L_p(\theta_{1t})L_q(\theta_{1t})\sigma_{pq}^{o2}(\theta_{1s},\phi_{1s};\theta_{1t},\phi_{1i}) \qquad (5)$$

σ_{pq}^{s1} and σ_{pq}^{s2} are the scattering terms from the top and the bottom surfaces, respectively. σ_{pq}^{o1} and σ_{pq}^{o2} are the respective bistatic scattering coefficients of those surfaces, based on the IEM rough surface model. θ_s and θ_i are scattered and incident angles in the air, and θ_{1s} and θ_{1i} are the corresponding angles in the layer. T_{10} and T_{01} are transmissivity from the top boundary into the layer and from the layer into the top boundary, respectively. L_p or L_q describes the attenuation of intensity through the layer. q is the incident field polarization, and p the scattered field polarization.

The bistatic scattering coefficient formulation used in the model is based on an existing IEM[7]. Several versions of the IEM are currently available[14-17]. In the present model, we used the original IEM accounting for both single and multiple scattering for the top and bottom surfaces.

This model was obtained from Fung[7] and given by

$$\sigma_{qp}^0(s) = \sigma_{qp}^k(s) + \sigma_{qp}^{kc}(s) + \sigma_{qp}^c(s) \qquad (6)$$

The first term is the Kirchhoff term, and accounts for single scattering only. It is given by

$$\sigma_{qp}^k(s) = 0.5k^2 \left| f_{qp} \right|^2 \exp\left[-\sigma^2(k_{sz} + k_z)^2\right]$$

$$\cdot \sum_{n=1}^{\infty} \frac{\left[\sigma^2(k_{kz} + k_z)^2\right]^n}{n!} W^{(n)}(k_{sx} - k_x, k_{sy} - k_y), \qquad (7)$$

where $k_x = k\sin\theta\cos\phi$, $k_y = k\sin\theta\sin\phi$, $k_z = k\cos\phi$, $k_{sx} = k\sin\theta_s\cos\phi_s$, $k_{sy} = k\sin\theta_s\cos\phi_s$, $k_{sz} = k\cos\phi_s$, k is the incident wavenumber, σ^2 is the variance of the surface, and $W^{(n)}$ is the nth power roughness spectrum.

The second term is the cross term. The single-sum terms are single scattering terms, and the double-sum term represents multiple scattering; it is given by

$$\sigma_{qp}^{kc}(s) = 0.5k^2 \exp\left[-\sigma^2(k_{sz}^2 + k_z^2 + k_z k_{sz})\right] \mathrm{Re}\{f_{qp} *$$

$$\left[F_{qp}(-k_x, -k_y) \sum_{n=1}^{\infty} \frac{\left[\sigma^2 k_{sz}(k_z + k_{sz})\right]^n}{n!} W^{(n)}(k_{sx} - k_x, k_{sy} - k_y) \right.$$

$$+ F_{qp}(-k_{sz}, -k_{sy}) \sum_{m=1}^{\infty} \frac{\left[\sigma^2 k_z(k_z + k_{sz})\right]^m}{m!} W^{(m)}(k_x - k_{sx}, k_y - k_{sy})$$

$$+ \frac{1}{2\pi} \sum_{n=1}^{\infty} \frac{\left[\sigma^2 k_{sz}(k_z + k_{sz})\right]^n}{n!} \sum_{m=1}^{\infty} \frac{\left[\sigma^2 k_z(k_z + k_{sz})\right]^m}{m!}$$

$$\iint F_{qp}(u,v) W^n(k_{sx} + u, k_{sy} + v) W^m(k_x + u, k_y + v) \mathrm{d}u\mathrm{d}v \left.\right]\} \qquad (8)$$

Finally, the third term is the complementary term. The single-scattering terms are again the terms with one sum. Multiple scattering is represented by terms with more than one sum, and is expressed as

$$\sigma_{qp}^c(s) = 0.125k^2 \exp\left[-\sigma^2(k_{sz}^2 + k_z^2)\right]$$

$$\cdot \left\{ \left| F_{qp}(-k_x, -k_y) \right|^2 \sum_{m=1}^{\infty} \frac{(\sigma^2 k_{sz}^2)^m}{m!} W^{(m)}(k_{sx} - k_x, k_{sy} - k_y) \right.$$

$$+ F_{qp}(-k_x, -k_y) F_{qp}*(-k_{sx}, -k_{sy})$$

$$\sum_{n=1}^{\infty} \frac{(\sigma^2 k_z k_{sz})^n}{n!} W^{(n)}(k_{sx} - k_x, k_{sy} - k_y)$$

$$+ F_{qp}*(-k_x, -k_y) F_{qp}(-k_{sx}, -k_{sy})$$

$$\sum_{m=1}^{\infty} \frac{(\sigma^2 k_z k_{sz})^m}{m!} W^{(m)}(k_{sx} - k_x, k_{sy} - k_y)$$

$$+ \left| F_{qp}(-k_{sx}, -k_{sy}) \right|^2 \sum_{n=1}^{\infty} \frac{(\sigma^2 k_z^2)^n}{n!} W^{(n)}(k_{sx} - k_x, k_{sy} - k_y)$$

$$+ \frac{1}{2\pi} \sum_{m=1}^{\infty} \frac{(\sigma^2 k_{sz}^2)^m}{m!} \sum_{n=1}^{\infty} \frac{(\sigma^2 k_z^2)^i}{i!}$$

$$\cdot \iint \left| F_{qp}(u,v) \right|^2 W^{(m)}(k_{sx} + u, k_{sy} + v) W^{(i)}(k_x + u, k_y + v) \mathrm{d}u\mathrm{d}v$$

$$+ \frac{1}{2\pi} \sum_{n=1}^{\infty} \sum_{m=1}^{\infty} \frac{(\sigma^2 k_z k_{sz})^{n+m}}{n!m!}$$

$$\cdot \iint F_{qp}(u,v) F_{qp}* \left[-(u + k_x + k_{sx}), -(v + k_y + k_{sy})\right]$$

$$\cdot W^{(n)}(k_{sx} + u, k_{sy} + v) W^{(m)}(k_x + u, k_y + v) \mathrm{d}u\mathrm{d}v\} \qquad (9)$$

Details of the formulation are in the paper by Fung[7].

3.2 Surface-volume scattering

In this model, the first-order surface-volume scattering term not included in Ewe et al.[2] was added in the theoretical modelling. More terms were derived from the second-order solution of the radiative transfer equation, to produce the second-order surface-volume scattering terms to be included in the modelling. The added first-order surface-volume scattering is given by

$$\sigma_{1pq}(\theta_s, \phi_s, \pi - \theta_i, \phi_i) =$$

$$\frac{\cos\theta_s}{4\pi} T_{01}(\theta_s, \theta_{1s}) T_{10}(\pi - \theta_{1i}, \pi - \theta_i) L_q^-(\theta_{1i}) L_p^+(\theta_{1s}) \sec\theta_{1s}$$

$$\int_0^{2\pi} \int_0^{\frac{\pi}{2}} \int_0^{2\pi} \int_0^{\frac{\pi}{2}} \sec\theta''\sin\theta'' \mathrm{d}\theta'' \mathrm{d}\phi'' \sec\theta'\sin\theta' \mathrm{d}\theta' \mathrm{d}\phi'$$

$$\sum_{t=v,h} \sum_{u=v,h} P_{tu}(\pi - \theta'', \phi'', \theta', \phi') \sigma_{uq}(\theta', \phi', \pi - \theta_{1i}, \phi_{1i})$$

$$\sigma_{pt}(\theta_{1s}, \phi_{1s}, \pi - \theta'', \phi'') \left[\frac{1 - L_u^+(\theta') L_t^-(\theta'')}{(K_{eu}^+ \sec\theta' + K_{et}^- \sec\theta'')} \right] \qquad (10)$$

where K_{eu} is the volume extinction coefficient. The other five derived terms are second-order solutions of Equation (1). The first and second terms are the volume-to-volume-to-surface interaction terms, and are expressed as

$$\sigma_{2pq}(\theta_s, \phi_s, \pi - \theta_i, \phi_i)$$

$$= \cos\theta_s \sec\theta_{1s} T_{10}(\pi - \theta_{1i}, \pi - \theta i) T_{01}(\theta_s, \theta_{1s})$$

$$\int_0^{2\pi} \int_0^{\frac{\pi}{2}} \sec\theta'\sin\theta' \mathrm{d}\theta' \mathrm{d}\phi'$$

$$\int_0^{2\pi} \int_0^{\frac{\pi}{2}} \sec\theta_\subset \sin\theta_\subset \mathrm{d}\theta_\subset \mathrm{d}\phi_\subset \sum_{t=v,h} \sum_{u=v,h}$$

$$P_{2tu}(\pi - \theta_\subset, \phi_\subset, \theta', \phi') P_{uq}(\theta', \phi', \pi - \theta_{1i}, \phi_{1i})$$

$$\sigma_{pt}(\theta_{1s}, \phi_{1s}, \pi - \theta_\subset, \phi_\subset) L_p^+(\theta_{1s}) L \qquad (11)$$

and

$$\sigma_{2pq}(\theta_s, \phi_s, \pi - \theta_i, \phi_i)$$

$$= \cos\theta_s \sec\theta_{1s} T_{01}(\theta_s, \theta_{1s}) T_{10}(\pi - \theta_{1i}, \pi - \theta i)$$

$$\int_0^{2\pi} \int_0^{\frac{\pi}{2}} \sec\theta'\sin\theta' \mathrm{d}\theta' \mathrm{d}\phi'$$

$$\int_0^{2\pi} \int_0^{\frac{\pi}{2}} \sec\theta_\subset \sin\theta_\subset \mathrm{d}\theta_\subset \mathrm{d}\phi_\subset \sum_{t=v,h} \sum_{u=v,h}$$

$$P_{2tu}(\pi - \theta_\subset, \phi_\subset, \pi - \theta', \phi') P_{uq}(\pi - \theta', \phi', \pi - \theta_{1i}, \phi_{1i})$$

$$\sigma_{pt}(\theta_{1s}, \phi_{1s}, \pi - \theta_\subset, \phi_\subset) L_p^+(\theta_{1s}) L \qquad (12)$$

The third term calculates the volume-to-surface-to-volume interaction, and is given by

$$\sigma_{2pq}(\theta_s,\phi_s,\pi-\theta_i,\phi_i) = \cos\theta_s \sec\theta_{1s}$$

$$T_{10}(\pi-\theta_{1i},\pi-\theta_i)T_{01}(\theta_s,\theta_{1s})$$

$$\int_0^{2\pi} d\phi_c \int_0^{\frac{\pi}{2}} \sec\theta_c \sin\theta_c d\theta_c \int_0^{2\pi} d\phi' \int_0^{\frac{\pi}{2}} \sec\theta' \sin\theta' d\theta'$$

$$\sum_{t=v,h}\sum_{u=v,h} P_{2pt}(\theta_{1s},\phi_{1s},\theta',\phi') P_{uq}(\pi-\theta_c,\phi_c,\pi-\theta_{1i},\phi_{1i})$$

$$\sigma_{tu}(\theta',\phi',\pi-\theta_c,\phi_c)\left[\frac{L_u^-(\theta_c)-L_q^-(\theta_{1i})}{(K_{eq}^- \sec\theta_{1i}+K_{eu}^- \sec\theta_c)}\right]$$

$$\left[\frac{L_t^+(\theta')-L_p^+(\theta_{1s})}{-K_{et}^+ \sec\theta'+K_{ep}^+ \sec\theta_{1s}}\right] \tag{13}$$

The last two derived terms are the surface-to-volume-to-volume interaction, and are given by

$$\sigma_{2pq}(\theta_s,\phi_s,\pi-\theta_i,\phi_i) = \cos\theta_s \sec\theta_{1s}$$

$$T_{10}(\pi-\theta_{1i},\pi-\theta_i)T_{01}(\theta_s,\theta_{1s})\sec\theta''$$

$$\int_0^{2\pi}\int_0^{\frac{\pi}{2}} \sec\theta'' \sin\theta'' d\theta'' d\phi'' \int_0^{2\pi}\int_0^{\frac{\pi}{2}} \sec\theta' \sin\theta' d\theta' d\phi'$$

$$\sum_{t=v,h}\sum_{u=v,h} P_{2pt}(\theta_{1s},\phi_{1s},\theta',\phi') P_{uq}(\theta',\phi',\theta'',\phi'')$$

$$\sigma_{tu}(\theta'',\phi'',\pi-\theta_{1i},\phi_{1i}) L_p^-(\theta_{1i}) \tag{14}$$

and

$$\sigma_{2pq}(\theta_s,\phi_s,\pi-\theta_i,\phi_i) = \cos\theta_s \sec\theta_{1s}$$

$$T_{10}(\pi-\theta_{1i},\pi-\theta_i)T_{01}(\theta_s,\theta_{1s})\sec\theta''$$

$$\int_0^{2\pi}\int_0^{\frac{\pi}{2}} \sec\theta' \sin\theta' d\theta' d\phi' \int_0^{2\pi}\int_0^{\frac{\pi}{2}} \sec\theta'' \sin\theta'' d\theta'' d\phi''$$

$$\sum_{t=v,h}\sum_{u=v,h} P_{2pt}(\theta_{1s},\phi_{1s},\pi-\theta',\phi') P_{uq}(\pi-\theta',\phi',\theta'',\phi'')$$

$$\sigma_{tu}(\theta'',\phi'',\pi-\theta_{1i},\phi_{1i}) L_p^-(\theta_{1i})L \tag{15}$$

3.3 Volume scattering

The volume scattering term from the first and second order solution of Equation (1) is shown in Ewe et al.[2] as

$$\sigma_{pq}^v = \sigma_{pq}^v(up,down) + \sigma_{pq}^v(up,up,down)$$

$$+\sigma_{pq}^v(up,down,down) \tag{16}$$

where

$$\sigma_{pq}^v(up,down) = 4\pi\cos\theta_s T_{01}(\theta_s,\theta_{1s})T_{10}(\pi-\theta_{1i},\pi-\theta_i)$$

$$\sec\theta_{1s} P_{pq}(\theta_{1s},\phi_{1s};\pi-\theta_{1i},\phi_{1i})$$

$$\cdot\frac{1-L_p(\theta_{1s})L_q(\theta_{1i})}{\kappa_{ep}(\theta_{1s})\sec\theta_{1s}+\kappa_{eq}(\theta_{1i})\sec\theta_{1i}} \tag{15}$$

$$\sigma_{pq}^v(up,up,down) = 4\pi\cos\theta_s T_{01}(\theta_s,\theta_{1s})T_{10}$$

$$(\pi-\theta_{1i},\pi-\theta_i)\sec\theta_{1s}\int_0^{2\pi} d\phi\int_0^{\pi/2}\sin\theta\sec\theta d\theta$$

$$\cdot\sum_{u=v,h}\left\{\frac{P_{pu}(\theta_{1s},\phi_{1s};\theta,\phi) P_{uq}(\theta,\phi;\pi-\theta_{1i},\phi_{1i})}{\kappa_{ep}(\theta_{1i})\sec\theta_{1i}+\kappa_{eu}(\theta)\sec\theta}\right.$$

$$\cdot\left[\frac{1-L_p(\theta_{1s})L_q(\theta_{1i})}{\kappa_{ep}(\theta_{1s})\sec\theta_{1s}+\kappa_{eq}(\theta_{1i})\sec\theta_{1i}}+\right.$$

$$\left.\left.\frac{L_q(\theta_{1i})\left[L_i(\theta)-L_p(\theta_{1s})\right]}{\kappa_{eu}(\theta)\sec\theta-\kappa_{ep}(\theta_{1s})\sec\theta_{1s}}\right]\right\} \tag{18}$$

$$\sigma_{pq}^v(up,down,down) = 4\pi\cos\theta_s T_{01}(\theta_s,\theta_{1s})T_{10}$$

$$(\pi-\theta_{1i},\pi-\theta_i)\sec\theta_{1s}\int_0^{2\pi} d\phi\int_0^{\pi/2}\sin\theta\sec\theta d\theta$$

$$\cdot\sum_{u=v,h}\left\{\frac{P_{pu}(\theta_{1s},\phi_{1s};\pi-\theta,\phi) P_{uq}(\pi-\theta,\phi;\pi-\theta_{1i},\phi_{1i})}{\kappa_{ep}(\theta_{1s})\sec\theta_{1s}+\kappa_{eu}(\theta)\sec\theta}\right.$$

$$\cdot\left[\frac{1-L_p(\theta_{1s})L_q(\theta_{1i})}{\kappa_{ep}(\theta_{1s})\sec\theta_{1s}+\kappa_{ep}(\theta_{1i})\sec\theta_{1i}}+\right.$$

$$\left.\left.\frac{L_q(\theta_{1s})\left[L_i(\theta)-L_p(\theta_{1i})\right]}{\kappa_{eu}(\theta)\sec\theta-\kappa_{ep}(\theta_{1i})\sec\theta_{1i}}\right]\right\} \tag{19}$$

4 Result and discussion

4.1 Theoretical analysis

Theoretical analysis is done by applying the developed model to a desalinated ice layer above thick saline ice. The desalinated ice layer is modelled as an irregular layer of pure ice with embedded air bubbles. The thick saline ice beneath the desalinated ice layer can be treated as a homogenous half space without inducing error, since the model only calculates the scattering process of the desalinated ice layer. For comparison purposes, the result from the model of Ewe et al.[2] is also included in all the figures. For ease of reference, this is referred to as the previous model, and the model developed herein as the new model. In the figures, results from these two models are referred to as those before and after, respectively. The effect of including multiple-surface scattering and surface-volume scattering up to second order is investigated by comparing the before and after results. The input parameters used are based on Fung[7], and listed in Table 1. The backscattering coefficient was calculated for a frequency of 5 GHz, over a range of incident angles from 10° to 70°. The effect of frequency, bottom surface roughness, and layer thickness on the contribution of surface multiple scattering and surface-volume scattering up to second order was investigated. This was done by varying the wave frequency, bottom-surface roughness that is the boundary between desalinated ice and salinated ice, and thickness of the desalinated sea-ice layer.

Table 1   Model parameters used in theoretical analysis

Parameters	Values used in model
Frequency/GHz	5
Scatterer radius/mm	0.5
Volume fraction/%	30
Effective relative permittivity of top layer	(1.0, 0.0)
Relative permittivity of sphere	(1.0, 0.0)
Background relative permittivity	(3.3, 0.000 1)
Lower half-space permittivity	(3.5, 0.25)
Thickness of layer/m	0.5
Top surface rms height and correlation length/cm	0.14, 0.7
Bottom surface rms height and correlation length/cm	0.16, 0.96

The frequency was first varied from 5 GHz to 1 GHz and 15 GHz. The backscattering coefficient was observed against incident angle for co-polarized (VV) and cross-polarized (VH) wave return. For VV polarization, there was no significant change observed between the previous and new models, at all frequencies. At 1 GHz and 5 GHz, total return was dominated by top-surface scattering. This result was expected, because in co-polarized surface backscattering, single-surface scattering is the important term, rather than multiple-surface scattering. At 15 GHz, volume scattering is dominant.
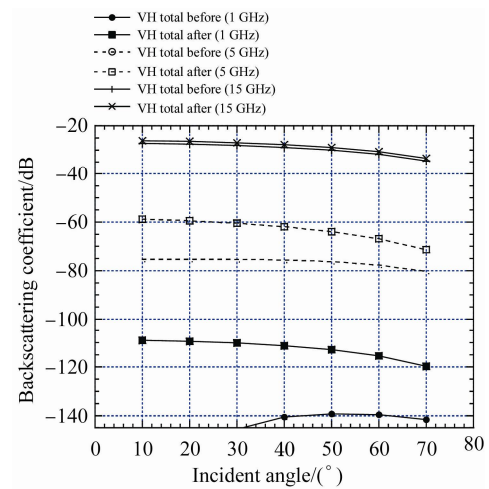
Figure 2 is a plot of total backscattering coefficient for VH polarizations at different frequencies. There was significant change between the previous and new model for 1 GHz and 5 GHz frequencies, and small change for 15 GHz. Each scattering component is shown in Figures 3 to 5.

For both top and bottom surface scattering, only the new model produced return. This is because cross-polarized return from surface backscattering is only from multiple-surface scattering; the contribution from single scattering is zero, since the single-scattering cross-polarized coefficient vanishes in the plane of incidence. The previous model did not produce return for top and bottom surface scattering, since it only considers single-surface scattering.

At 1 GHz, total backscatter was dominated by top-surface scattering, with some contribution from bottom-surface scattering. This indicates that improvement in total backscatter was from the contribution of multiple-surface scattering. At 5 GHz, the contribution from the bottom surface became less important, since there is more wave interaction in the sea-ice layer. For surface-volume scattering, there was improvement from the new model, owing to the added terms. Therefore, improvement of total backscatter at 5 GHz was due to the contribution from multiple scattering on the top surface and surface-volume scattering up to second order. At 15 GHz, sea ice becomes too lossy, so volume scattering becomes dominant. The small difference in total backscattering coefficient between the previous and new models was due to the contribution from surface-volume scattering up to second order. Further in-

crease in frequency shows that surface-volume scattering continues to be an important scattering component after volume scattering, until volume scattering totally dominates above a frequency about 17 GHz.

These results show that surface multiple scattering is very important in cross-polarized backscattering for calculating the contribution of surface scattering. Including surface multiple scattering and additional surface-volume scattering terms up to second order improves the total cross-polarized backscattering coefficient in the lower frequency region, where surface and surface-volume scattering contributions are important.

Figure 2   Total backscattering coefficient (VH polarization) against incident angle for various frequencies.
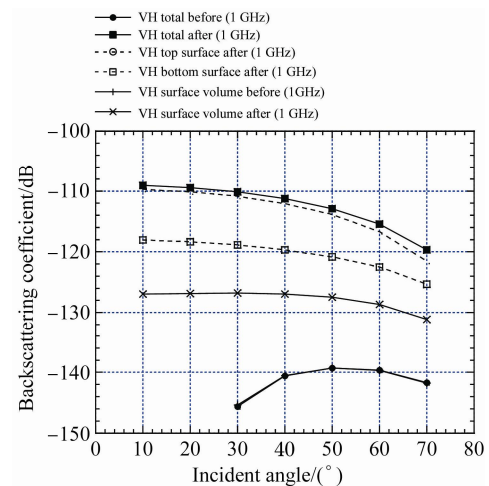
Figure 3   Backscattering coefficient for each backscattering component (VH polarization) against incident angle at 1 GHz frequency.

Next, roughness of the boundary between desalinated ice and salinated ice was varied by changing its standard deviation of surface height variation (RMS height) normalized by frequency k_σ, from 0.16 to 0.05 and 0.3. The backscattering coefficient is plotted against incident angle for co-polarized and cross-polarized wave return.
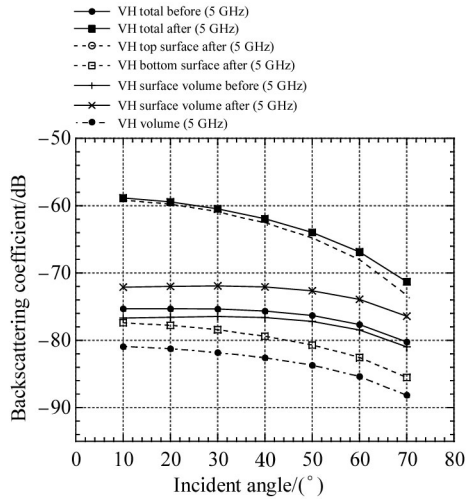
Figure 4 Backscattering coefficient for each backscattering component (VH polarization) against incident angle at 5 GHz frequency.
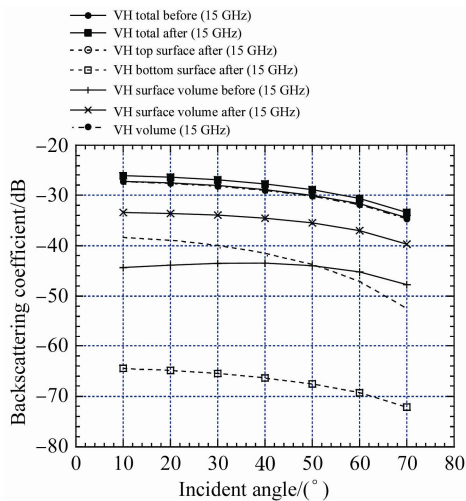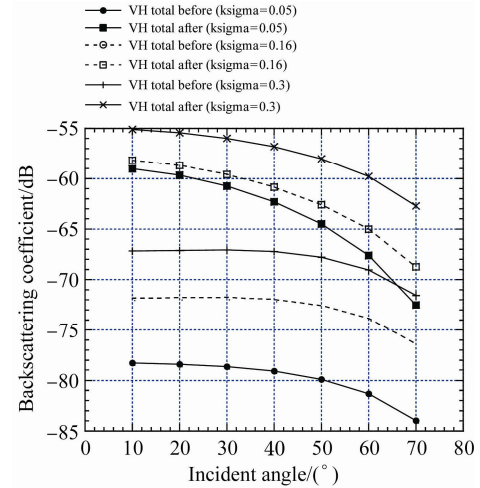

Figure 5 Backscattering coefficient for each backscattering component (VH polarization) against incident angle at 15 GHz frequency.

It is seen that for VV polarization, there was no significant change between the previous and new models for all bottom-surface $k\sigma$. Since the top surface is the dominant scattering mechanism, there is no difference between the two models as expected, since co-polarized surface backscattering is dominated by single scattering.

Figure 6 shows a plot of total backscattering coefficient for VH polarization. It is seen that there was significant change between the previous and new models for all bottom-surface $k\sigma$. Contributions from the top surface, bottom surface, surface-volume, and volume scattering for VH backscatter were examined for each $k\sigma$, and are shown in Figures 7 to 9. When the bottom surface $k\sigma$ was 0.05, the total backscattering coefficient was dominated by top-surface scattering, with some contribution from surface-volume scattering and volume scattering. A significant difference is evident between the two models for sur-

face-volume scattering. Therefore, improvement of the total backscattering coefficient was mainly from the top-surface multiple scattering, enhanced by surface-volume scattering up to second order.

Figure 6 Total backscattering coefficient (VH polarization) against incident angle for various $k\sigma$ of bottom surface.

When $k\sigma$ of the bottom surface was 0.16, the contribution of surface-volume scattering increased. The dominant scattering mechanism remained top-surface scattering but, as the incident angle increased, the surface-volume contribution became important. Therefore, improvement of the total backscattering coefficient with bottom-surface roughness $k\sigma$=0.16 was from the top-surface multiple scattering and surface-volume scattering up to second order.

With $k\sigma$=0.3, the bottom-surface contribution further increased and became the main scattering component. The surface-volume scattering contribution also increased, with the same difference between the two models. Multiple-surface scattering on both the top and bottom surfaces, along with surface-volume scattering up to second order, improved the total backscattering coefficient significantly for that surface roughness.

By analyzing the backscatter return for different roughnesses of the boundary between the desalinated ice and salinated ice, it was revealed that for the sea-ice case, multiple-surface scattering and surface-volume scattering up to second order are important in cross-polarized backscattering calculation for all surface roughnesses.

Finally, the thickness of the desalinated sea ice was varied by changing its layer thickness from 0.5 m to 0.1 m and 1 m. The backscattering coefficient is plotted against incident angle for co-polarized and cross-polarized wave returns.
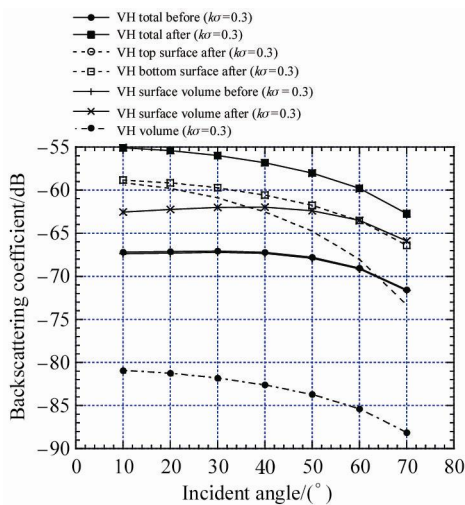
For VV polarization, there was no significant change between the previous and new models for all the layer thickness. This is expected, since the top-surface scattering was dominant for all layer thicknesses, with significant contribution from bottom-surface scattering.
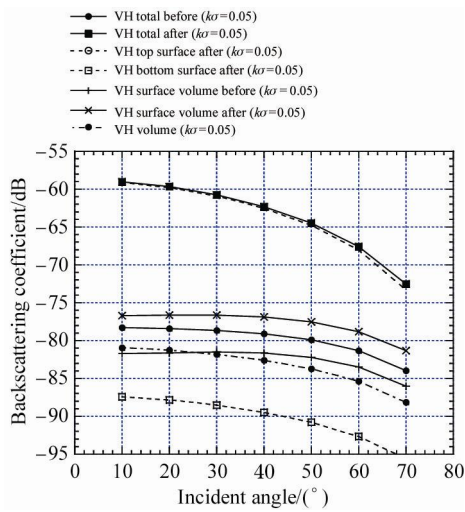
Figure 7 Backscattering coefficient for each backscattering component (VH polarization) against incident angle at bottom surface $k\sigma$=0.05.
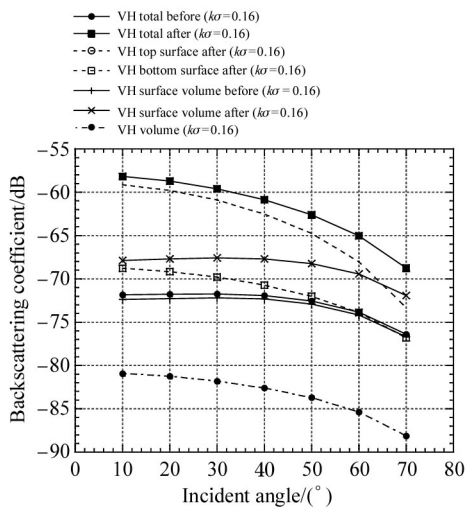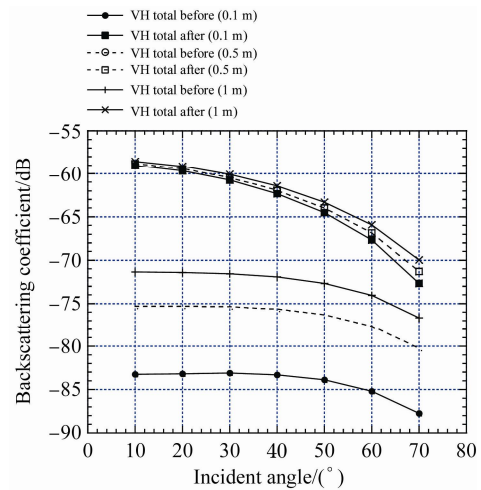

Figure 8 Backscattering coefficient for each backscattering component (VH polarization) against incident angle at bottom surface $k\sigma$=0.16.

Figure 9 Backscattering coefficient for each backscattering component (VH polarization) against incident angle at bottom surface $k\sigma$=0.3.

Figure 10 is a plot of total backscattering coefficient for VH polarizations and different layer thicknesses. It is seen that there was significant change between the previous and new models for all layer thicknesses. Contributions from the top surface, bottom surface, surface-volume, and volume scattering for VH backscatter were investigated for each layer thickness, and are shown in Figures 11 to 13. For layer thickness 0.1 m, Figure 11 shows that the total backscattering coefficient was dominated by the top surface, with a slight contribution from surface-volume. There was significant improvement in the surface-volume scattering contribution in the new model. Therefore, the difference between the two models for total backscattering was largely from multiple scattering on the top surface, enhanced by surface-volume scattering up to second order. For layer thicknesses 0.5 m and 1 m, with the same improvement for surface-volume scattering in the new model, the contribution from surface-volume scattering increased, owing to increased scattering in the layer. Top-surface scattering remained the dominant mechanism.

Therefore, by increasing layer thickness from 0.1 m to 1 m, the total backscatter was dominated by multiple scattering on the top surface, with an increasing contribution from surface-volume scattering up to second order. These results show that the new model is important for cross-polarized backscattering, for all layer thicknesses.
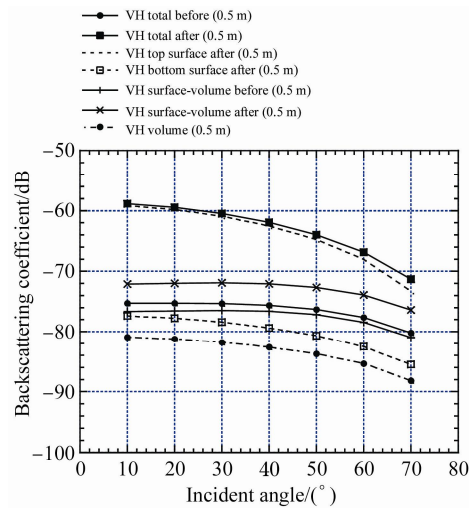

Figure 10 Total backscattering coefficient (VH polarization) against incident angle for various layer thicknesses, *d*.

Theoretical analysis of sea ice shows that surface multiple scattering and surface-volume scattering up to second order are very important in cross-polarized backscattering when there is a contribution from surface scattering and surface-volume scattering, but less important in co-polarized backscattering. For cross-polarized surface scattering, only the new model gives return, since the contribution from cross-polarized surface backscattering is only from the surface multiple-scattering process. By increasing any of the parameters of wave frequency, bottom surface $k\sigma$ and layer thickness, within the range studied, the contribution from surface-volume scattering increases. The new model does not improve the total backscattering coefficient when the scattering mechanism is dominated by volume scattering.
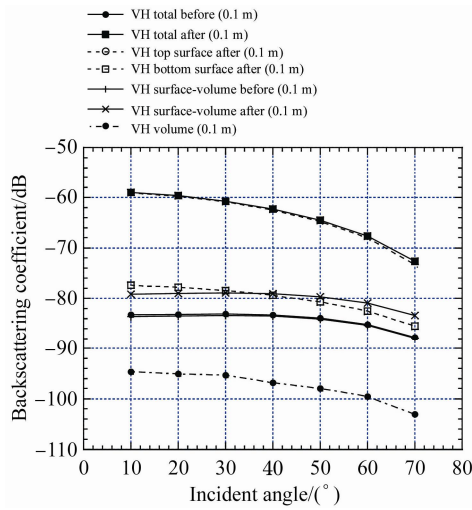
Figure 11 Backscattering coefficient for each backscattering component (VH polarization) against incident angle at layer thickness *d*=0.1 m.
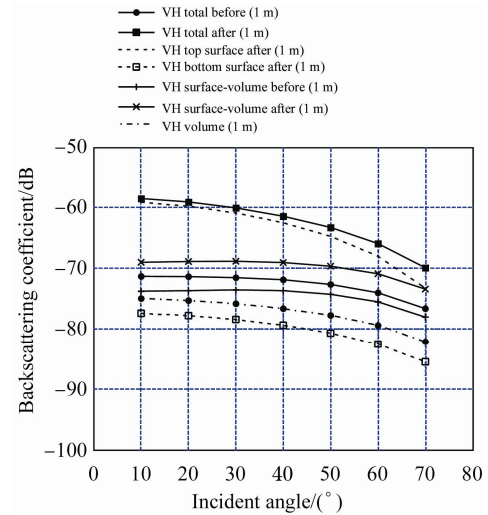
4.2 Comparison with measurement results

To ensure model reliability, the developed theoretical model was validated using ground-truth measurement data. Measurement data from sea ice were input to the model. The results were then compared with satellite and the ground-truth data.

For co-polarized backscattering in sea ice, ground-truth measurements from 2006 at Cape Evans on Ross Island in Antarctica were used, and model prediction was compared with RADARSAT data. The measurement data used for model simulation are summarized in Table 2. Figure 14 shows the HH-polarized backscattering coefficients of the new and previous models, and backscattering coefficients obtained from RADARSAT imagery. Although there was no difference between the new and previous models as expected, there was good agreement between the measured data and theoretical results.

For cross-polarized backscattering, we used backscattering measurements on multiyear sea ice during 1988 and
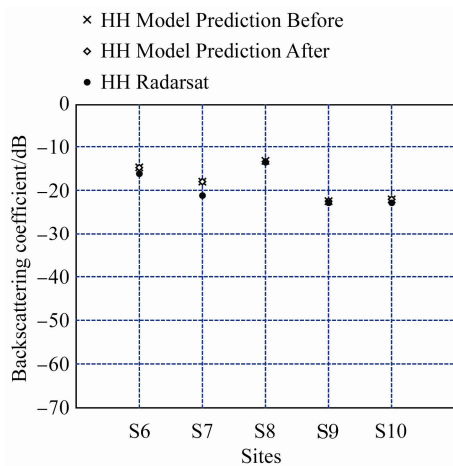

Figure 12 Backscattering coefficient for each backscattering component (VH polarization) against incident angle at layer thickness *d*=0.5 m.

Figure 13 Backscattering coefficient for each backscattering component (VH polarization) against incident angle at layer thickness *d*=1 m.

Table 2 Parameter detail for sea ice sites in 2006

| Parameters	Values used in model				
	S6	S7	S8	S9	S10
Scatterer Radius/m			2.50×10^{-4}		
Volume fraction/%	4.06	3.33	4.63	2.76	3.41
Effective relative permittivity of top layer			(1.0, 0)		
Relative permittivity of scatterer	49.05, 41.03	49.28, 41.28	50.01, 41.98	49.20, 41.19	49.32, 41.32
Background relative permittivity	3.59, 1.64	3.50, 1.38	3.66, 1.94	3.44, 1.12	3.51, 1.41
Relative permittivity of bottom layer	58.75, 43.87	58.62, 44.01	58.65, 43.98	58.68, 43.95	58.65, 43.98
Thickness of layer/m	1.56	1.68	1.57	1.6	1.6
Top surface rms height and correlation length/m	2.76×10^{-3}, 19.56×10^{-3}	2.04×10^{-3}, 27.52×10^{-2}	3.54×10^{-3}, 31.43×10^{-3}	1.36×10^{-3}, 7.57×10^{-3}	1.36×10^{-3}, 7.57×10^{-3}
Bottom surface rms height and correlation length/m			$(2.80 \times 10^{-4}, 2.10 \times 10^{-2})$		

Figure 14   HH-polarized backscattering coefficient of model prediction and RADARSAT.

Table 3   Parameter details for CEAREX site alpha-35

Parameters	Alpha-35	
Scatterer radius/mm	0.8	
Volume fraction of scatterer/%	11	
Relative permittivity of top layer	1.0 , 0.0	
Relative permittivity of scatterer	1.0, 0.0	
Background relative permittivity	3.20	-1.10×10^{-2}
Relative permittivity of bottom layer	3.50	-0.25
Layer thickness/m	0.14	
Top surface RMS and correlation length/m	0.35×10^{-2}	4.56×10^{-2}
Bottom surface RMS and correlation length/m	0.35×10^{-2}	4.56×10^{-2}
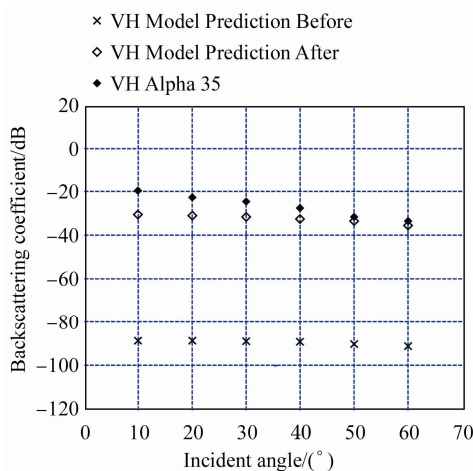
Figure 15   VH-polarized backscattering coefficient of model prediction and CEAREX measurement.

1989 winter segments of the Coordinated Eastern Artic Experiment (CEAREX)[18]. One of the sites (Alpha-35) was selected for the comparison. Parameter details of the sites are summarized in Table 3. Figure 15 shows VH-polarized backscattering coefficient from the new and previous models, and the backscattering coefficient from CEAREX measurement. Compared with the previous model prediction, the new model gives significant improvement. Since top-surface scattering is the dominant scattering mechanism in the area, the previous model, which does not calculate cross-polarized return for surface scattering, does not give sufficiently accurate prediction. Compared with the CEAREX measurement, the new model prediction is generally correct, except at small incidence angles. The higher measured values at small incidence angles may be attributed to antenna pattern effects[19].

5   Conclusion

A reliable theoretical model to study sea ice is presented in this paper. The model was developed by including multiple-surface scattering and surface-volume scattering up to second order, as in Ewe et al[2]. Theoretical analysis was done by applying the model to a sea-ice layer, and improvement in backscattering return was evaluated for different frequencies, surface roughness and layer thickness. This analysis showed that surface multiple-scattering and surface-volume scattering up to second order are very important in cross-polarized backscattering, but less important in co-polarized backscattering, in the range studied. Comparison with field measurements was also done to validate the model. Results show a good match between theoretical prediction and satellite data for co-polarized return, and a promising match for cross-polarized return. Future work includes extension of the surface scattering formulation to the advanced IEM (AIEM)[17] and consideration of a multilayer model[20].

References

1   Lee Y J, Lim W K, Ewe H T. A study of an inversion model for sea ice thickness retrieval in Ross Island, Antarctica. Prog Electromagn Res, 2011, 111: 381-406.

2   Ewe H T, Chuah H T, Fung A K. A backscatter model for a dense discrete medium: analysis and numerical results. Remote Sensing of Environment, 1998, 65(2): 195-203.

3   Chandrasekhar S. Radiative transfer. New York: Dover Publications, 1960.

4   Syahali S. A study of surface and surface-volume scattering. Saarbrücken, Germany: LAP Lambert Academic Publishing, 2012.

5   Syahali S, Ewe H T, Ibrahim S A. Theoretical modeling and analysis of multiple surface scattering and surface-volume scattering in snow layer // AKEPTs 1st annual young researchers conference and exhibition (AYRC X3 2011). Kuala Lumpur: AYRC, 2011.

6   Syahali S, Ewe H T. Model development and analysis of multiple surface scattering and surface-volume scattering in sea ice layer//IEEE Asia-Pacific Conference on Applied Electromagnetics (APACE 2012). Melaka, Malaysia: IEEE, 2012: 22-27.

7   Fung A K. Microwave scattering and emission models and their applications. Norwood, MA: Artech House, 1994: 164-275.

8   Ewe H T, Chuah H T. A study of dense medium effect using a simple backscattering model // Proceedings of IEEE International Geoscience and Remote Sensing Symposium. Singapore: IEEE, 1997, 3: 1427-1429.

9   Chuah H T, Tjuatja S, Fung A K, et al. A phase matrix for a dense discrete random medium: evaluation of volume scattering coefficient. IEEE Transactions on Geoscience Remote Sensing, 1996, 34(5): 1137-1143.

10   Chuah H T, Tjuatja S, Fung A K, et al. Radar backscatter from a dense discrete random medium. IEEE Transactions on Geoscience and Remote Sensing, 1997, 35(4): 892-899.

11   Wen B, Tsang L, Winebrenner D P, et al. Dense medium radiative transfer theory: Comparison with experiment and application to microwave remote sensing and polarimetry. IEEE Transactions on Geoscience and Remote Sensing, 1990, 28(1): 46-59.

12   Ishimaru A, Kuga Y. Attenuation constant of a coherent field in a dense distribution of particles. J Opt Soc America, 1982, 72(10): 1317-1320.

13   Fung A K, Eom H J. A study of backscattering and emission from closely packed inhomogeneous media. IEEE Transactions on Geosciences and Remote Sensing, 1985, GE-23(5): 761-767.

14   Fung A K, Liu W Y, Chen K S, et al. An improved IEM model for bistatic scattering from rough surfaces. J Electromagnet Wave, 2002, 16(5): 689-702.

15   Álvarez-Pérez J. An extension of the IEM/IEMM surface scattering model. Wave Random Med, 2001, 11(3): 307-329.

16   Wu T D, Chen K S. A reappraisal of the validity of the IEM model for backscattering from rough surfaces. IEEE Transactions on Geoscience and Remote Sensing, 2004, 42(4): 743-753.

17   Wu T D, Chen K S, Shi J C, et al. A study of an AIEM model for bistatic scattering from randomly rough surfaces. IEEE Transactions on Geoscience and Remote Sensing, 2008, 46(9): 2584-2598.

18   Grenfell T C. Surface-based passive microwave studies of multiyear sea ice. J Geophys Res, 1992, 97(C3): 3485-3501.

19   Fung A K, Eom H J. Coherent scattering of a spherical wave from an irregular surface. IEEE Transactions on Antennas and Propagation, 1983, 31(1): 68-72.

20   Albert M D, Lee Y J, Ewe H T, et al. Multilayer model formulation and analysis of radar backscattering from sea ice. Prog Electromagn Res, 2012, 128: 267-290.